ADVANCES IN ATMOSPHERIC SCIENCES, VOL. 40, MAY 2023, 900–919

• **Original Paper** •

Assimilation of FY-3D MWTS-II Radiance with 3D Precipitation Detection and the Impacts on Typhoon Forecasts※

Luyao QIN[1], Yaodeng CHEN*[1], Gang MA*[2], Fuzhong WENG[2], Deming MENG[1], and Peng ZHANG[3]

[1]*Key Laboratory of Meteorological Disaster of Ministry of Education (KLME)/Joint International Research Laboratory of Climate and Environment Change (ILCEC)/Collaborative Innovation Center on Forecast and Evaluation of Meteorological Disasters (CIC-FEMD), Nanjing University of Information Science & Technology, Nanjing* 210044, *China*

[2]*Earth System Modeling and Prediction Centre, China Meteorological Administration, Beijing* 100081, *China*

[3]*Key Laboratory of Radiometric Calibration and Validation for Environmental Satellites (LRCVES/CMA), National Satellite Meteorological Center, China Meteorological Administration (NSMC/CMA), Beijing* 100081, *China*

(Received 2 July 2021; revised 14 December 2021; accepted 7 January 2022)

ABSTRACT

Precipitation detection is an essential step in radiance assimilation because the uncertainties in precipitation would affect the radiative transfer calculation and observation errors. The traditional precipitation detection method for microwave only detects clouds and precipitation horizontally, without considering the three-dimensional distribution of clouds. Extending precipitation detection from 2D to 3D is expected to bring more useful information to the data assimilation without using the all-sky approach. In this study, the 3D precipitation detection method is adopted to assimilate Microwave Temperature Sounder-2 (MWTS-II) onboard the Fengyun-3D, which can dynamically detect the channels above precipitating clouds by considering the near-real-time cloud parameters. Cycling data assimilation and forecasting experiments for Typhoons Lekima (2019) and Mitag (2019) are carried out. Compared with the control experiment, the quantity of assimilated data with the 3D precipitation detection increases by approximately 23%. The quality of the additional MWTS-II radiance data is close to the clear-sky data. The case studies show that the average root-mean-square errors (RMSE) of prognostic variables are reduced by 1.7% in the upper troposphere, leading to an average reduction of 4.53% in typhoon track forecasts. The detailed diagnoses of Typhoon Lekima (2019) further show that the additional MWTS-II radiances brought by the 3D precipitation detection facilitate portraying a more reasonable circulation situation, thus providing more precise structures. This paper preliminarily proves that 3D precipitation detection has potential added value for increasing satellite data utilization and improving typhoon forecasts.

Key words: numerical weather prediction, radiance assimilation, microwave temperature sounding, FY-3D MWTS-II, precipitation detection

Citation: Qin, L. Y., Y. D. Chen, G. Ma, F. Z. Weng, D. M. Meng, and P. Zhang, 2023: Assimilation of FY-3D MWTS-II radiance with 3D precipitation detection and the impacts on typhoon forecasts. *Adv. Atmos. Sci.*, **40**(5), 900–919, https://doi.org/10.1007/s00376-022-1252-x.

Article Highlights:

- The precipitation detection for satellite radiances is extended from 2D to 3D space with a dynamic channel selection method.
- With the 3D precipitation detection, the amount of assimilated FY-3D MWTS-II data is greatly increased without increasing observation error.
- The 3D precipitation detection shows the potential value added for typhoon track and intensity analysis and forecasts.

1. Introduction

Satellite microwave (MW) and infrared (IR) sounding instruments provide high-resolution measurements of atmospheric temperature and humidity from the troposphere to the middle and upper stratosphere (Eyre et al., 2020), especially in areas where conventional observations are rare. Bene-

※ This paper is a contribution to the special issue on the 14th International Conference on Mesoscale Convective Systems and High-Impact Weather.

* Corresponding authors: Yaodeng CHEN, Gang MA
Emails: keyu@nuist.edu.cn, magang@cma.gov.cn

fiting from the development of radiative transfer models, data assimilation methods, as well as a large number of operational meteorological satellites in service (Saunders et al., 1999; Buehner et al., 2010; Bauer et al., 2015), satellites observations have become an indispensable part of numerical weather prediction (NWP). The assimilation of satellites radiances contributes significantly to global (Zhou et al., 2010; Guidard et al., 2011) and regional (Wang et al., 2015, 2017; Xie et al., 2019) NWP skills.

Because of the complexity of radiative transfer calculations under precipitation conditions and the limitations of the physics parameterization of models, the assimilation of precipitation-affected radiances can be challenging. In general, the radiance assimilation is carried out after discarding these radiances by precipitation detection; this is called a "clear-sky" radiance assimilation. To make better use of radiance information, the method of direct "all-sky" radiance assimilation in the presence of cloud and precipitation was pioneered at the European Centre for Medium-Range Weather Forecasts (ECMWF) (Bauer et al., 2010) decades ago. Several operational centers have adopted the all-sky assimilation approach, leading to significant positive impacts on medium-range forecasts (Geer et al., 2018). As one of the most valuable observations in global operational forecasting (Geer et al., 2019), MW temperature radiances have been assimilated with the all-sky approach by only a few operational centers (Geer et al., 2017). One concern is that cloud-related errors could adversely affect the temperature fields and destroy the analysis (Geer et al., 2019). Many studies on MW temperature all-sky assimilation (Zhu et al., 2016; Migliorini and Candy, 2019; Weston et al., 2019; Tong et al., 2020) have adopted a similar approach, assigning larger observation errors in cloudy and precipitation areas (Geer and Bauer, 2011) dependent on cloud estimates. Therefore, even in the most advanced all-sky approach, the detection of clouds and precipitation is indispensable.

For MW temperature sounders, the traditional methods that rely on the low-frequency window channels of 23.8 GHz, 31.4 GHz, and 89 GHz have facilitated the investigation of cloud and precipitation detection. For example, Grody et al. (2001) and Weng et al. (2003) retrieved liquid water paths (LWP) through 23.8 GHz and 31.4 GHz channels to determine whether the pixels were affected by precipitation. Notable progress has been made in the assimilation of Advanced Microwave Sounding Unit-A (AMSU-A) and Advanced Technology Microwave Sounder (ATMS) radiances using these methods (Weng et al., 2007; Zou et al., 2013). But the calculation of LWP is difficult for the Microwave Temperature Sounder (MWTS) onboard the Fengyun-3 (FY-3, Zhang et al., 2019b) series meteorological satellite, although it has similar channel settings and sounding characteristics to AMSU-A and has been employed successfully in NWP (Lu et al., 2011; Zhang et al., 2019a; Carminati et al., 2021). Since low-frequency window channels are not included in MWTS, an imaging assistance method was investigated. This method is based on the cloud cover (CC), which is provided by the Visible Infrared Radiometers (VIRR) onboard the same platform (Li and Zou, 2013; Li and Liu, 2016b). Researchers have demonstrated that this is an effective way of assimilating MWTS clear radiances (Li and Zou, 2014; Li and Liu, 2016a), which has been adopted operationally by the Global/Regional Assimilation and PrEdiction System (GRAPES) of the China Meteorological Administration (CMA).

It should be noted that the retrieval of LWP and the imager-assisted method mentioned above only detect clouds and precipitation horizontally, when in fact, clouds vary in the vertical direction as well. If this vertical structure can be identified, the cloud can be detected more accurately, and observations around clouds will be more appropriately applied. To make better use of observations not affected by precipitation, Qin et al. (2020) developed the dynamic channel selection (DCS) method as a three-dimensional precipitation detection method for the MWTS-II onboard FY-3D by considering the near 3D real-time cloud distribution. The impacts of CC and cloud top height (CTH) on the simulated brightness temperature (BT) were analyzed through sensitivity experiments, and lookup tables were subsequently established. The channels above the precipitation clouds could be considered as clear-sky channels and selected based on the lookup tables. The impact of the radiances above precipitation on analyses and forecasts has not been evaluated.

The aim of this work is to further explore the potential of the DCS method in assimilation application. As mentioned above, all-sky MW temperature assimilation is still full of challenges. Therefore, extending precipitation detection from 2D to 3D is expected to bring more useful information to the data assimilation system without using the all-sky approach. A simplified observing system and a regional model configuration were adopted in this study. The remainder of the paper is organized as follows: Section 2 briefly introduces the 3D precipitation method, FY-3D MWTS-II data, and preprocessing steps. Section 3 introduces the typhoon cases and experiment design. Section 4 conveys the impact of the 3D precipitation method on FY-3D MWTS-II data quality and coverage. The results of the analysis and forecast are described in section 5. The Typhoon Lekima (2019) case is analyzed in detail in section 6. The summary and discussion are given in section 7.

2. Methods and data

2.1. *The 3D precipitation detection method*

The fast radiative transfer models, e.g., the Radiative Transfer for TIROS Operational Vertical Sounder TOVS (RTTOV) and the Community Radiative Transfer Model, allow rapid cross-conversion of model variables to BT and serve as the observation operator role in data assimilation. However, strong absorption of cloud liquid water (CLW) and scattering of ice clouds and precipitation lead to large errors in the BT simulation. Therefore, removing observations affected by clouds is necessary before radiance data assimilation. The 3D precipitation detection is achieved by

dynamic selection of clear-sky channels above precipitation, called the DCS method. Under clear-sky conditions, the radiative transfer equation for channel i can be written as follows:

$$L_{i,\mathrm{clr}} = \varepsilon_{i,\mathrm{sur}}\tau_{i,\mathrm{sur}}B(T_\mathrm{s})_i + \int_{P_\mathrm{sur}}^{P_\mathrm{top}} B(T)_i \frac{\partial \tau_i}{\partial p}\mathrm{d}p + (1-\varepsilon_{i,\mathrm{sur}})\tau_{i,\mathrm{sur}}^2 \int_{P_\mathrm{sur}}^{P_\mathrm{top}} \frac{B(T)_i}{\tau_i^2}\frac{\partial \tau_i}{\partial p}\mathrm{d}p\,, \quad (1)$$

where $L_{i,\mathrm{clr}}$ is clear radiance, $\varepsilon_{i,\mathrm{sur}}$ is the surface emissivity, $B(T)_i$ is the Planck function, $\tau_{i,\mathrm{sur}}$ is the surface-to-space transmittance, T_s is the surface temperature, P_top is the top layer of pressure coordination used in RTTOV, and P_sur is the surface pressure. τ_i is the cumulative transmittance of all absorbing gases from the model layer to space and can be presented as below:

$$\tau_i = \exp\left(-\sum_{j=1}^{n}\sum_{k=1}^{m} a_{i,j,k}X_{j,k}\right), \quad (2)$$

where $a_{i,j,k}$ are the transmittance coefficients, $X_{j,k}$ are the predictors, m and n are the number of absorbing gases and pressure coordination layers defined by RTTOV respectively, and k and j are the kth and jth of those. If a non-precipitation cloud has thickness and exists in many layers, the radiance transfer equation should be written as below:

$$L_i = (1-N)L_{i,\mathrm{clr}} + NL_{i,\mathrm{cld}}\,, \quad (3)$$

where L_i is total radiance, $L_{i,\mathrm{cld}}$ is cloudy radiance, and N is the fractional cloud cover. For those channels whose weighting function peak heights are already higher than the cloud top height, the absorptions in clouds are strong, and the transmissions below the clouds are small. Therefore, only the transmission of absorbing gases from cloud top to space could be contained in the radiative transfer calculation, while the cloudy radiance $L_{i,\mathrm{cld}}$ can be written as follows:

$$L_{i,\mathrm{cld}} = \int_{P_\mathrm{cld\_top}}^{P_\mathrm{top}} B(T)_i \frac{\partial \tau}{\partial p}\mathrm{d}p\,, \quad (4)$$

where $P_\mathrm{cld\_top}$ is the cloud top pressure. Under this condition, the CLW absorption should be considered for MW radiance. CLW should be added as one of the absorbing gases, and an additional calculation for CLW transmittance is added:

$$\tau_\mathrm{clw} = \exp\left(\sum_{j=\mathrm{mw\_cldtop}}^{\mathrm{nlevs}} 4.5 f^2 X_{j,\mathrm{clw}} \frac{Z_\mathrm{b}}{(2+Z_\mathrm{a})^2 + Z_\mathrm{b}^2}\right), \quad (5)$$

where $X_{j,\mathrm{clw}}$ are the CLW predictors associated with the satellite zenith angle, f is the central frequency of the channel, nlevs is the number of model layers, and mw_cldtop is the top layer of clouds in the CLW profile. Z_a and Z_b are empirical coefficients related to frequency. The lack of a calculation for the CLW transmittance in the clear-sky assimilation can cause large simulation errors. The sensitivity of each channel to CLW is different, and the impact of CLW on simulation errors is also different. The DCS method takes these into account and analyzes the difference between total radiance and clear-sky radiance, which can be written as below:

$$\begin{aligned}\mathrm{diff} &= L_i - L_{i,\mathrm{clr}} = [(1-N)L_{i,\mathrm{clr}} + \mathrm{N}L_{i,\mathrm{cld}}] - L_{i,\mathrm{clr}} \\ &= N(L_{i,\mathrm{cld}} - L_{i,\mathrm{clr}})\,. \end{aligned} \quad (6)$$

Qin et al. (2020) analyzed the influence of CC and CTH on the diff values through RTTOV9.2 and established the lookup tables based on different diff values for 54.4 GHz, 54.94 GHz, and 55.5 GHz. For a given pixel, the accuracy for the simulated BT of which channel is affected by the CC and CTH can be determined according to the lookup tables, and the contaminated channels of this pixel can be simultaneously removed. But MW sounders cannot retrieve CC and CTH directly, so it is necessary to obtain CC and CTH in MW pixels by a pixel-remapping technique with the help of an IR imager onboard the same satellite platform. It is worth noting that the differences in optical properties between IR and MW make IR more cloud-sensitive than MW. Clouds that can affect IR radiances do not always affect MW radiances to the same extent, which may lead to overestimation in cloud-affected MW radiances through IR observations. But it can ensure that the MW radiances that have passed the IR-assistant detection are more likely clear. Since the weighting function peaking height of 53.596 GHz is only 700 hPa, it is much more sensitive to cloud water than other channels. Therefore, the 53.596 GHz channel is not discussed in this study because it is strongly unaffected by low clouds. Three thresholds (0.05 K, 0.1 K, and 0.2 K) of diff values are selected to determine the accuracy of the simulated BT in Qin et al. (2020), whereas 0.05 K was chosen for this study because of the similar impacts from the three thresholds.

2.2. *FY-3D MWTS-II data and preprocessing*

FY-3D, an afternoon-orbit satellite of the Chinese Fengyun series, was launched in November 2017. The MWTS-II onboard FY-3D has 13 channels in the 50–60 GHz oxygen absorption band and can provide atmospheric temperature information from the surface to 2 hPa. There are 90 FOVs in each scanline with a horizontal resolution of approximately 32 km. The swath width is 2250 km. The central frequency, weighting function peak heights, bandwidth, and noise equivalent differential temperature (NE$\triangle T$) of the FY-3D MWTS-II are shown in Table 1 (Carminati et al., 2021). In this study, the Level-1c (L1c) products from the FY-3D MWTS-II were provided by the National Satellite Meteorological Centre (NSMC) of the CMA. According to the Medium Resolution Spectral Imager (MERSI) -2 cloud product, the CC and CTH required by the DCS method are already remapped in the L1c dataset and can be obtained from the operational CMA NWP center in near-real time.

To prevent the assimilation of poor-quality data, necessary preprocessing is required for raw radiance data before

Table 1. The channel characteristics of FY-3D MWTS-II.

Channel Numbers	Central frequency (GHz)	Weighting function peak heights (hPa)	Bandwidth (MHz)	NE△T (K)
1	50.3	Surface	180	0.3
2	51.76	Surface	400	0.2
3	52.8	950	400	0.2
4	53.596	700	400	0.23
5	54.40	400	400	0.2
6	54.94	270	400	0.2
7	55.50	180	330	0.3
8	57.290344	90	330	0.4
9	Fo±0.217	50	78	0.5
10	Fo±0.3222±0.048	20	36	0.5
11	Fo±0.3222±0.022	12	16	0.7
12	Fo±0.3222±0.010	5	8	1.2
13	Fo±0.3222±0.0045	2	3	1.5

Note: Fo=57.290344.

assimilation, including bias correction, quality control, and preliminary channel selection. Significant systematic biases between the observations and the first guess exist due to the inaccuracies in the radiative transfer model and the instrument 's characteristics. The Variational Bias Correction (VarBC) method, which has been proven to minimize the analysis disruptions (Auligné and McNally, 2007), was used here to correct the systematic biases. The VarBC method expresses the bias as a linear combination of predictors that can be updated adaptively during the minimization of variational analysis. By running a VarBC "off-line" model with 25-day (from 1 to 25 August 201) radiance data, the bias correction coefficient and predictor statistics are obtained for the first cycle analysis. The predictors include 1000–300 hPa and 200–50 hPa layer thickness, surface skin temperature, total column water vapor, the scan position, and the square and cube of scan position. Then, the bias correction coefficients are updated from the previous analysis output.

Quality control (Zhang et al., 2019b) includes (1) outlier detection: the radiances are removed when OMBs (observation minus background) exceed either 15 K or three times the standard deviations (STDV) of the observation error, whichever is smaller, (2) surface type detection: radiances binned into mixed surface-type are removed, (3) scan position check: the data of the eight outermost FOVs are removed, and (4) pressure detection: the observations from channel 5 are removed when the surface pressure is smaller 850 hPa to reduce the influence of the plateau terrain.

Moreover, not all MWTS-II channels are suitable for assimilation. As shown in Table 1, channels 1 and 2 are sensitive to the surface. Channels 3 and 4 are sensitive to CLW and the surface due to their primary goal of measuring lower-troposphere atmospheric temperatures. These channels are not assimilated in this study because the lack of accurate surface emissivity makes it difficult to simulate the corresponding BT accurately. Channels 9–13 are mainly aimed at upper-stratosphere atmospheric temperatures. Accurate atmospheric state profiles with corresponding heights from the first guess are needed to assimilate these channels, which is a challenge for this study because of the model's top setting at 10 hPa. Thus, channels 9–13 are also excluded to avoid excessive simulation errors.

3. Typhoons, model, and experiments

3.1. *Overview of typhoon cases*

Two typhoon cases were selected for the evaluation. Typhoon Lekima (2019) was the strongest typhoon that hit China in 2019. Typhoon Lekima (2019) developed from a tropical depression at 0600 UTC 2 August in the western Pacific and moved slowly toward the northwest. The tropical depression strengthened into a tropical storm at 0600 UTC 4 August and became a typhoon at 1200 UTC 6 August. Then, the typhoon continued to move northwestward and landfall in Zhejiang Province, China, at 1745 UTC 9 August. The maximum wind speed (MWS) of Lekima (2019) was 84 kt (1 kt ≈ 0.514 m s^{-1}) with the central sea level pressure (CSLP) at 935 hPa at the time of landfall. After landfall, Lekima (2019) moved northward across eastern China. It stayed on land for as long as 44 h and brought heavy precipitation, resulting in more than 14 million people being affected and more than 51.53 billion RMB in economic losses.

Typhoon Mitag (2019) moved quickly and turned offshore. Mitag (2019) was a weak typhoon, so its forecast was more challenging. Typhoon Mitag (2019) formed at 0000 UTC 28 September 2019 in the western Pacific. It moved toward the northwest and strengthened into a Typhoon at 0600 UTC 29 September, then made landfall in Zhejiang Province, China, at 1230 UTC 1 October with an MWS of 60 kt. Then, Typhoon Mitag (2019) turned to the northeast and made a second landfall on the coast of South Korea at 1200 UTC 2 October. Typhoon Mitag (2019) caused major losses to the countries along its track. The best tracks of these typhoons from the Joint Typhoon Warning Center (JTWC) are shown in Fig. 1.

3.2. *Model configuration*

The Advanced Research Weather Research and Forecasting (ARW-WRF) model version 4.1 and WRF model data assimilation (WRFDA) systems are used for both experiments. The WRFDA version 4.1 is modified to allow the assimilation of MWTS-II radiances in this study. Moving, triple-nested grids are configured for all experiments, as shown in Fig. 1. The innermost domain can follow the movement of a typhoon automatically. With the highest resolution, a better simulation of both the track and intensities of a typhoon can be achieved.

The horizontal grid spacing is 27 km, 9 km, and 3 km with 240 × 200, 325 × 325, and 274 × 274 grid points (lon.× lat.) for the outside domain (D01), the middle domain (D02), and the moving domain (D03), respectively. All three domains are configured with 57 vertical levels with a 10-hPa model top. The Global Forecast System (GFS) of NCEP 1° × 1° analysis is used as the initial and boundary conditions for D01, which has not assimilated MWTS-II before. The assimilation is only performed at D01 to include as much MWTS-II radiance data as possible to provide better initial and boundary conditions for the smaller domains. The initial values of D02 and D03 come from the interpolation of D01, so that the information of MWTS-II can be passed to the smaller domains directly. The raw radiance data are thinned on a 60-km grid to minimize potential correlations between adjacent observations (Liu and Rabier, 2002) while retaining as many observations as possible in the typhoon region.

The following physical parameterizations are adopted: the WRF Single-Moment 6-class scheme (WSM6) microphysics scheme (Hong and Lim, 2006), the Rapid Radiative Transfer Model for GCMs (RRTMG) shortwave and longwave radiation schemes (Iacono et al., 2008), the Yonsei University (YSU) boundary layer scheme (Hong et al., 2006), the Monin-Obukhov surface layer scheme, the unified Noah land-surface model, and the Tiedtke cumulus parameterization scheme (Tiedtke, 1989).

The CV7 scheme is adopted for the background error covariance matrix (***B***), using the U-V for the dynamic control variable (Sun et al., 2016). Forecast differences from ARW-WRF between the 12- and 24-h forecasts, valid at the same time for one month (0000 UTC 1 August to 0000 UTC 30 August 2019), are used to calculate the ***B*** based on the National Meteorological Centre (NMC) method (Parrish and Derber, 1992).

3.3. *Experimental design*

To demonstrate the feasibility of the DCS method on MWTS-II radiance assimilation and forecasting, two cycling forecast-analysis experiments are designed on a simplified observing system. Both experiments assimilate conventional observations and MWTS-II radiance, and the MWTS-II data preprocessing steps are performed as described in section 2.3. The difference between the two experiments is the precipitation detection scheme. After bias correction and quality control, the control (CTRL) experiments use the precipitation detection method developed by Li and Liu (2016b), which is coded in the Global/Regional Assimilation and PrEdiction System (GRAPES) and carried out operationally in

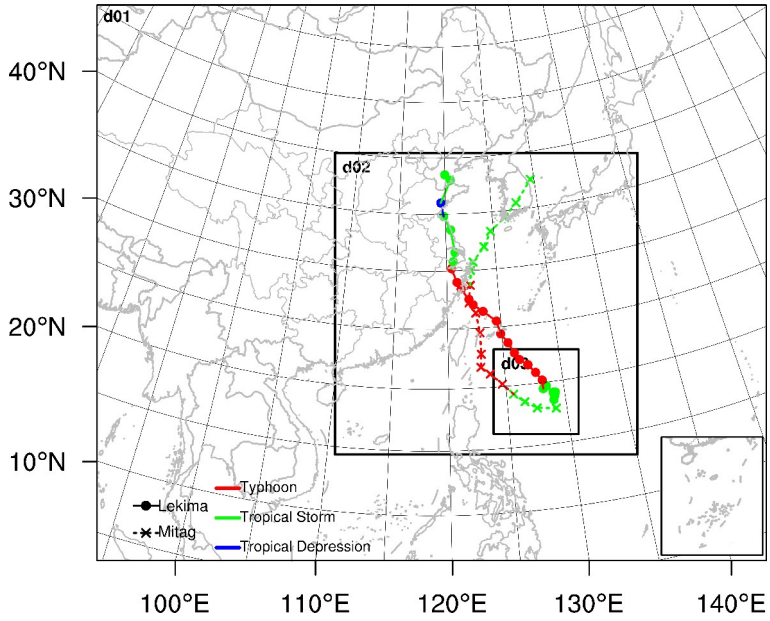

Fig. 1. The experimental domains and the best tracks of Typhoons Lekima (2019, solid line) and Mitag (2019, dashed line) from the Joint Typhoon Warning Center (JTWC). Lines with different colors indicate the different stages of a typhoon as defined by JTWC; blue for tropical depression, green for tropical storm, and red for typhoon. The locations for the start of experiments are indicated as orange.

the CMA. Only CC is used as a reference in the CTRL experiments. When the CC is larger than 0.76, the observation is rejected. The DCS experiment uses the DCS method based on the lookup table, which comprehensively considers the distribution of CC and CTH and removes observations affected by clouds.

In this study, partial cycles (Hsiao et al., 2012) are initiated at 0600 UTC daily, which means that the first guess at 0600 UTC is a 6-h forecast from 0000 UTC each day. Partial cycles could correct the large-scale circulation bias through the cold start and reduce the systematic mode errors accumulated during cycle assimilation and model integration. Then, the assimilation runs four times at 0600 UTC, 1200 UTC, 1800 UTC, and 0000 UTC daily with a 6-h cycle. For each analysis cycle, the data within ±3 hours of the analysis times are assimilated, and a 72-h forecast is carried out respectively. The experiment for Lekima (2019) is initiated at 0600 UTC 6 August, and that for Mitag (2019) is initiated at 0600 UTC 29 September, before they were declared typhoons. The forecasts ended at 0000 UTC 11 August for Lekima (2019) and 0000 UTC 3 October for Mitag (2019).

4. Impacts of the DCS method on the data

4.1. *Data amount and quality*

The quantity and quality of observations directly affect the assimilation. To assess the impact of the DCS method on the quality of observations, the scatter plots for all observations and background BT during all the assimilation cycles of the two typhoon cases are shown in Figs. 2a–b, d–e, and g–h. The histogram plots of OMB statistics for all observations after bias correction and quality control are shown in Figs. 2c, f, and i. The black dots indicate the data did not pass the quality controls, and the blue and red dots indicate the data were assimilated for CTRL and DCS experiments, respectively. All the experiments begin with 55 245 observations, but only part of those observations enter the assimilation system. The quality control process removes many outliers from the set of observations, especially observations of BT with low values. After quality control, these outliers and large biases are removed. Similar to the CTRL experiments, observed and background BTs in the DCS experiments are

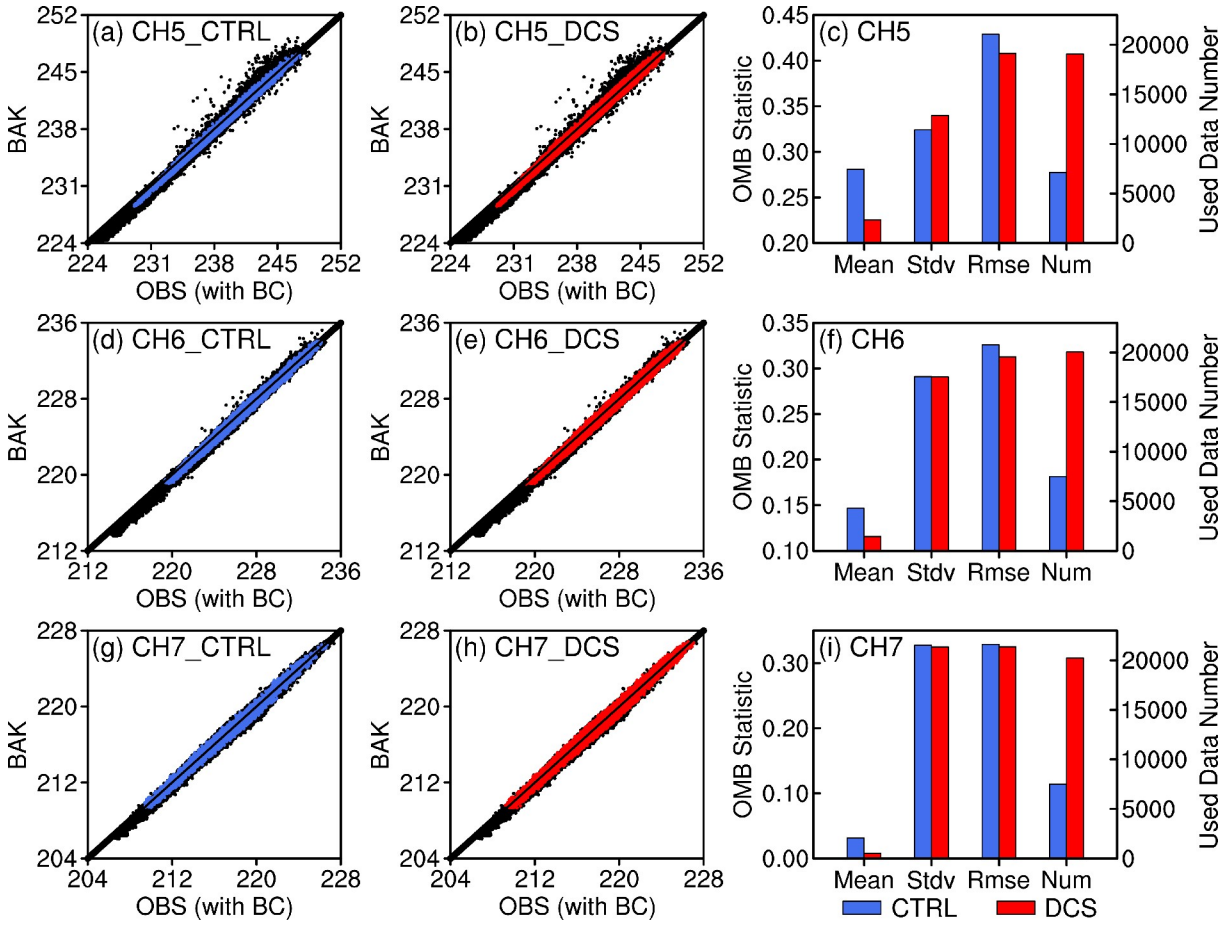

Fig. 2. The scatter plots for all observations and the simulated brightness temperature for the two typhoon cases for MWTS-II channels 5–7 in (a), (d), and (g) CTRL experiments and (b), (e), and (h) DCS experiments. The black dots indicate the data did not pass the quality controls, and the blue and red dots indicate that the data were used in data assimilation by the CTRL and DCS experiments, respectively. The histogram plots for mean, standard deviations (STDVs), root-mean-squares (RMSs), and number of OMB for MWTS-II channels (c) 5, (f) 6, and (i) 7. The blue and red columns indicate the CTRL and DCS experiments, respectively.

also very close, but the amount of data used is more than twice that of the CTRL experiments. The DCS method does not introduce additional outliers, even with a larger number of data points, which would benefit the assimilation. For the statistics of OMB, the number of observations available for data assimilation in channels 5–7 increases gradually (from less than 20 000 to more than 20 000), corresponding to the decreased sensitivity to CLW. There are approximately 2–3 times more observations in the DCS experiment than in the CTRL experiment, which increases the data utilization rate from about 13% to 36%.

In general, the DCS experiment has a mean closer to zero than the CTRL experiment, indicating that the OMB bias in the DCS experiment is small. The STDVs and root-mean-squares (RMSs) in the DCS experiments are smaller than those in the CTRL experiments, except for channel 5. The reasons for a larger STDV in channel 5 are complicated and may include the emissivity error due to the complexity of surface type, the background forecast error, and the possibility of cloud contamination. In particular, channel 5 is the most surface-sensitive out of the three assimilated channels. Some of the radiances that passed in the DCS experiments may not be suitable for assimilation, i.e., in a region where surface emissivity has larger uncertainties. Quality control is crucial for radiance assimilation. It is essential to implement strict quality control while increasing the number of observations. To prevent impacts from the complicated surface, additional quality controls can be added, such as using the surface emissivity Jacobian or the surface skin temperature Jacobian as quality control parameters (Lee et al., 2019). In addition, there is also a possibility of observations being contaminated by clouds. It might be inaccurate to choose the same diff threshold for all three channels. A stricter diff threshold should be beneficial to reduce cloud contamination or other potential problems. However, the OMB statistics of both CTRL and DCS experiments have the same order of magnitude. The slight increase in STDV of the DCS experiment for channel 5 is about 0.015 and does not exceed the variation range of STDV at different assimilation cycles (not shown). The observations error would not increase as the number of observations increases.

Probability density function (PDF) distributions of OMB after bias correction are shown in Fig. 3. The blue lines indicate CTRL experiments, and the red lines indicate DCS experiments. An important assumption of variational assimilation is that the OMB is unbiased and subject to a Gaussian distribution. It can be seen that all lines show an approximately Gaussian distribution, which should be suitable for assimilation, although there still are some residual biases, especially in channel 5. Compared to the CTRL experiments, the bias of the DCS experiments is closer to zero. To quantify the distance between two distributions and Gaussian distribution, it is possible to calculate their relative entropy, or Kullback-Leibler (K-L) distance (Migliorini and Candy, 2019). In the discrete univariate case, the K-L distance of $p_i(x)$ and $q_i(x)$ can be written as:

$$d_{\mathrm{KL}} = \sum_i p_i(x) \log\left[\frac{p_i(x)}{q_i(x)}\right], \tag{7}$$

which gives the sample mean [according to $p_i(x)$] difference of the logarithm of $p_i(x)$ and the logarithm of $q_i(x)$. In this study, the sample mean differences between the OMB PDF and the Gaussian PDF are calculated and marked in Fig. 3. For all three channels, the d_{KL} values in the DCS experiments are closer to zero and indicate the PDF of OMB is more Gaussian. Since the bias correction procedure used in this study is not optimized for MWTS-II with striping noise, the d_{KL} is larger than that of Migliorini and Candy (2019) for AMSU-A. However, in general, the PDF distributions in the DCS experiments are more symmetrical, which indicates that the Gaussianity of the OMB is not compromised, even if the observations of the DCS experiments have increased. The additional observations from the DCS experiments are reasonable and reliable.

4.2. *Coverage of assimilated data*

Since channel 7 has the largest number of observations,

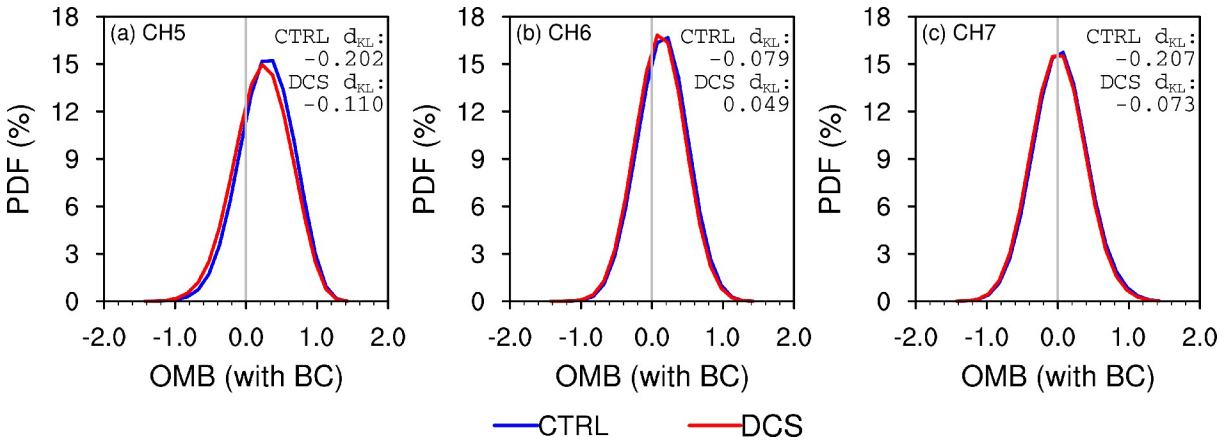

Fig. 3. The probability density distribution (PDF) of OMB after bias correction for MWTS-II channels 5–7. The blue and red lines indicate the CTRL and DCS experiments, respectively. The d_{KL} is a measure of distance between these two distributions and Gaussian distribution.

only channel 7 is selected to demonstrate the data coverage. The coverage of the observations used in the assimilation (green dots) for typhoons Lekima (2019) (top) and Mitag (2019) (bottom) is shown in Fig. 4. The BT of the FY-3D MERSI-2 12-μm channel is depicted as a gray background to indicate the distribution of clouds. It can be seen that for the two typhoon cases, the DCS experiments have more observations than the CTRL experiments. The additional observations for DCS experiments are mainly distributed in cloudless areas or at the edges of clouds, while few observations are in areas with strong convection and complex cloud phases, such as the typhoon inner core. Coverage of observations is closely related to real-time cloud distribution. The coverages of remapped CC and CTH are shown in Fig. 5. The cloudless area corresponds to a smaller remapped CC value and a lower CTH. However, it is apparent that observations have been excluded in some areas that appear to be cloudless because of missing CTH data. The locations of missing CTH correspond to higher BT in MESRI-2, which indicates that the clouds may be sparse, and the CTH could be difficult to determine. Such an observation is set as missing data to ensure the accuracy of the remapped CTH. This phenomenon is more evident in the Typhoon Lekima (2019) case, which also explains why the number of observations for the Lekima (2019) case is smaller than for the Mitag (2019) case. The pixel remapping process still requires further quality improvement.

5. Impacts of the DCS method on the forecast results

5.1. *Verification against ERA5*

To quantitatively evaluate the impact of MWTS-II on analysis and forecasting with the DCS method, the analysis fields and forecast fields of the two cases are verified against ECMWF Re-Analysis 5 (ERA5) (Hersbach et al., 2020). ERA5 does not use the MWTS-II on FY-3D. The cycle-averaged root-mean-square error (RMSE) of temperature, relative humidity, *U*-wind, and *V*-wind for the 48-h deterministic forecasts in model domain 2 (see Fig. 1) are calculated, and the results for the upper (200 hPa), middle (500 hPa), and lower (850 hPa) troposphere are shown in Fig. 6 and Fig. 7 for Typhoon Lekima (2019) and Typhoon Mitag (2019) respectively. Eight groups of forecasts for the Lekima (2019) case and four groups of forecasts for the Mitag (2019) case are used in the verification. In general, the RMSEs of each variable in the upper troposphere are larger than those in the lower troposphere, and the RMSEs increase with the forecast lead time. To quantify the impacts, the improve ratio (in %) can be defined as:

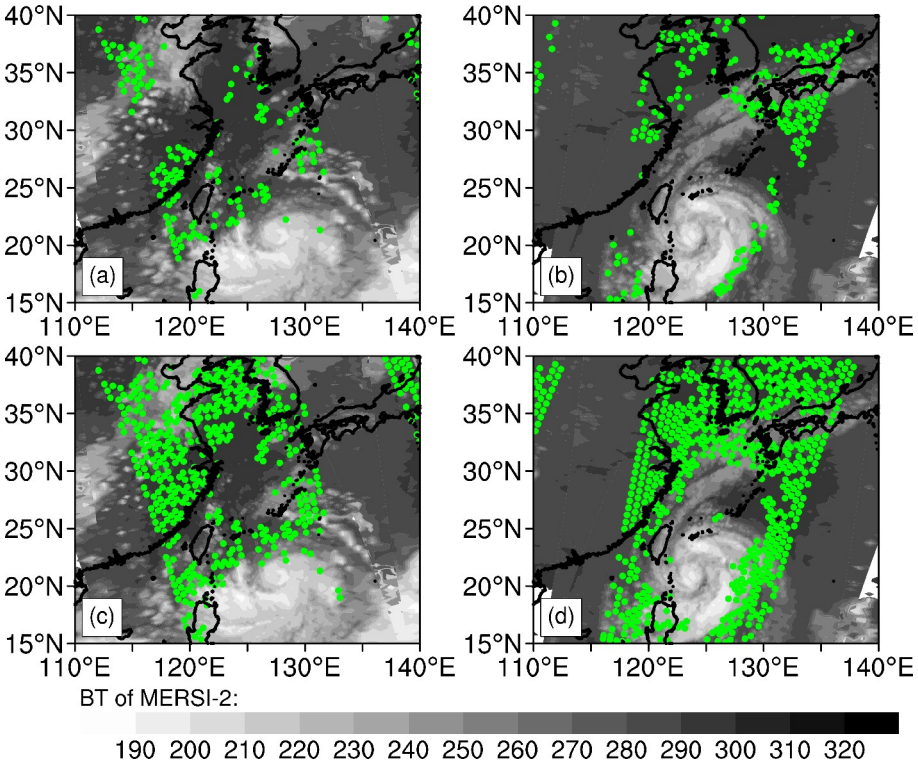

Fig. 4. The coverage of the observations (green dots) used in data assimilation for channel 7 in the (a), (b) CTRL, and (c), (d) DCS experiments. The brightness temperature of the FY-3D MERSI-2 12-μm channel is depicted as a gray background to indicate the distribution of clouds. The time of data distribution is (a), (c) 0600 UTC 7 August 2019 [for Typhoon Lekima (2019)] and (b), (d) 1800 UTC 29 September 2019 [for Typhoon Mitag (2019)], respectively.

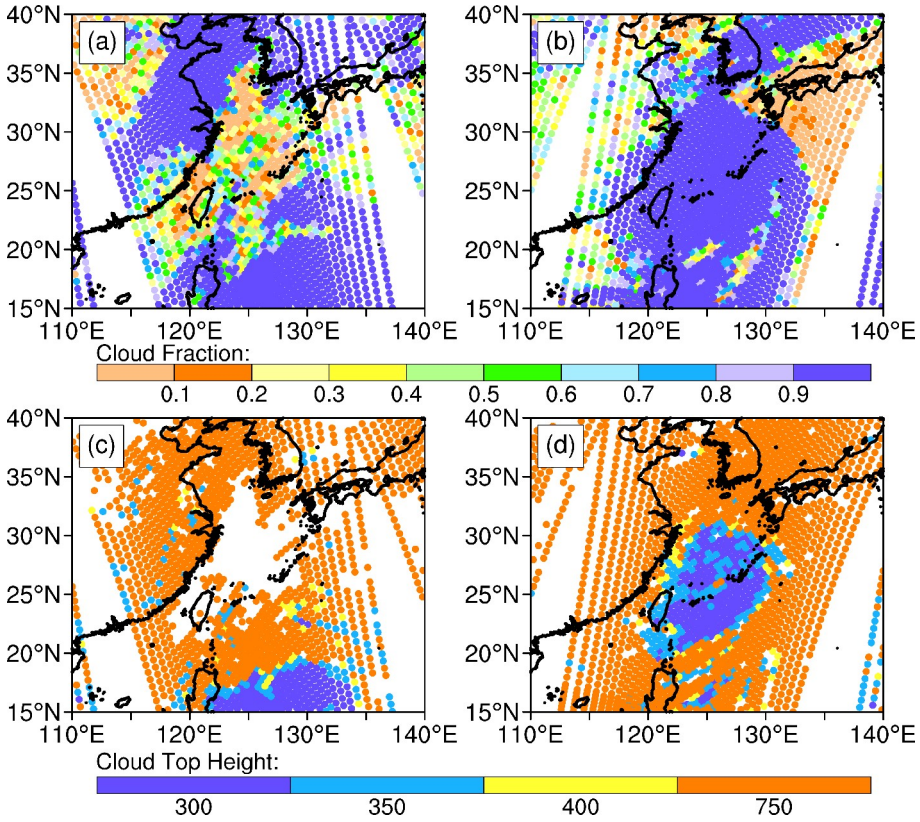

Fig. 5. The remapped cloud parameters required by the DCS method; (a), (b) remapped cloud fraction, and (c), (d) remapped cloud top height. The time of remapped cloud parameters distribution is (a), (c) 0600 UTC 7 August 2019 [for Typhoon Lekima (2019)] and (b), (d) 1800 UTC 29 September 2019 [for Typhoon Mitag (2019)], respectively.

$$\text{Ratio}_{\text{Improve}} = \frac{\text{RMSE}_{\text{CTRL}} - \text{RMSE}_{\text{DCS}}}{\text{RMSE}_{\text{CTRL}}} \times 100\,, \qquad (8)$$

and is calculated for every 6-h forecast. The averaged results at different levels are shown in Table 2.

For temperature in the middle and upper troposphere, the average RMSEs in the DCS experiments are slightly reduced compared to those in the CTRL experiments; but the average RMSEs are increased in the lower layers. This decreasing trend is most evident in the Mitag (2019) case at 200 hPa (Fig. 7a), where the average improve ratio is 2.42%. RMSE reduction may benefit from more upper channels being assimilated.

For relative humidity, the RMSEs of the DCS and CTRL experiments are relatively close. In the Lekima (2019) case, the RMSEs of the DCS experiment show a slight increase at 200 hPa and at 850 hPa. In the Mitag (2019) case, the DCS experiment shows slight improvements. As a temperature-sounding instrument, the assimilation of additional MWTS-II radiance data produces limited improvement for relative humidity.

However, the improvement of the *U*- and *V*-wind component RMSEs with the DCS method is obvious, especially at 200 hPa. The relative change between the DCS and CTRL experiments increases with the forecast lead time. The average improve ratio is 0.99% for Lekima (2019) and 1.45% for Mitag (2019) for 200-hPa *U*-wind. For 200-hPa *V*-wind, the values are 1.49% and 1.20%, respectively. The reason for the improvement in the wind forecast is related to the cycle assimilation scheme. As a MW-temperature sounder, MWTS-II is assimilated to provide a noticeable increment in temperature analysis. At the same time, the other model variables of analysis fields (model initial values), such as surface pressure and geopotential height, can also be updated after assimilation. Through cycle assimilation, these model initial values are continuously updated, and the information from observation is transferred to other forecast variables (e.g., wind, etc.) through the dynamical constraints of the dynamic equations of atmospheric motion. After several cycles, this improvement gradually accumulates and becomes evident. Similar results can also be found in Li and Liu (2016b) and other studies. At the same time, because of the large forecast errors of wind, its improvements are obvious. In fact, the improve ratios of wind and temperature are on the same order of magnitude (see Table 2).

The profiles of the averaged RMSEs at different forecast times are shown in Fig. 8, and similar conclusions can be made. The impacts of the DCS method become more evident as the deterministic forecast time extends. The improvement of temperature is mainly concentrated above 500 hPa, and the improvement in the wind field is more evident than temperature due to the larger wind forecast error. The average

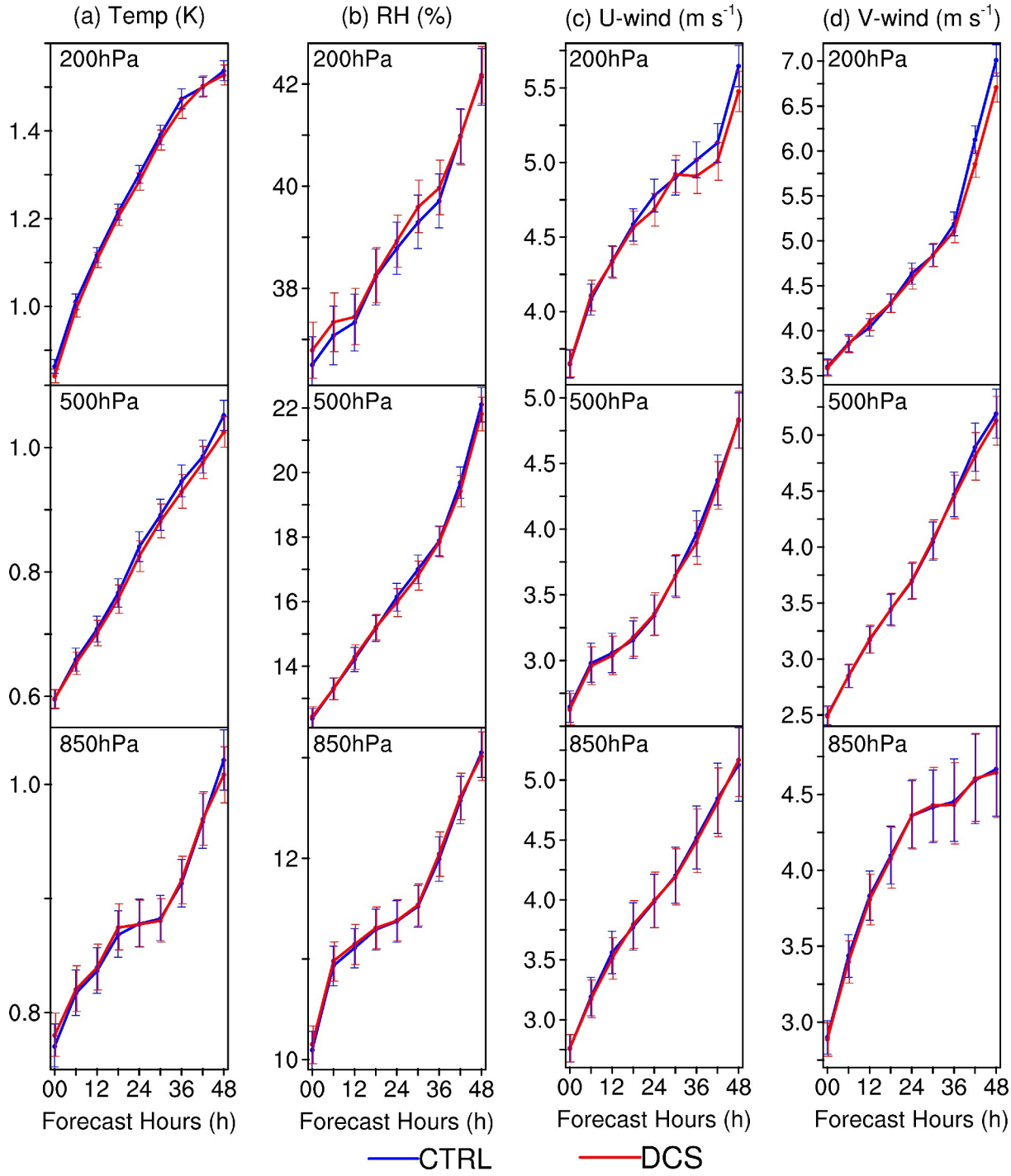

Fig. 6. The cycle-averaged root-mean-square error (RMSE) of (a) temperature, (b) relative humidity, and (c) *U*- and (d) *V*-wind 48-h deterministic forecasts for Typhoon Lekima (2019). The blue lines indicate CTRL experiments, and the red lines indicate DCS experiments. Error bars show the confidence interval of the mean RMSE for 95% confidence limit. confidence limit.

improvement rates of these four prognostic variables in the upper, middle, and lower troposphere are 1.7%, 0.5%, and 0.05%, respectively.

The error bars in Fig. 6 and Fig. 7 show the 95% confidence interval. For the Lekima (2019) case, the differences between the experiments were not statistically significant. For the Mitag (2019) case, some statistically significant results can be found in temperature and *V*-wind at 200 hPa. Significant differences between the CTRL and DCS experiments are concentrated only in the upper troposphere, where the average improvement in temperature and wind is 1.5%. The DCS method brings limited improvement, probably because only one MW sounder was assimilated with the DCS approach. As a polar-orbiting satellite, FY-3D has a

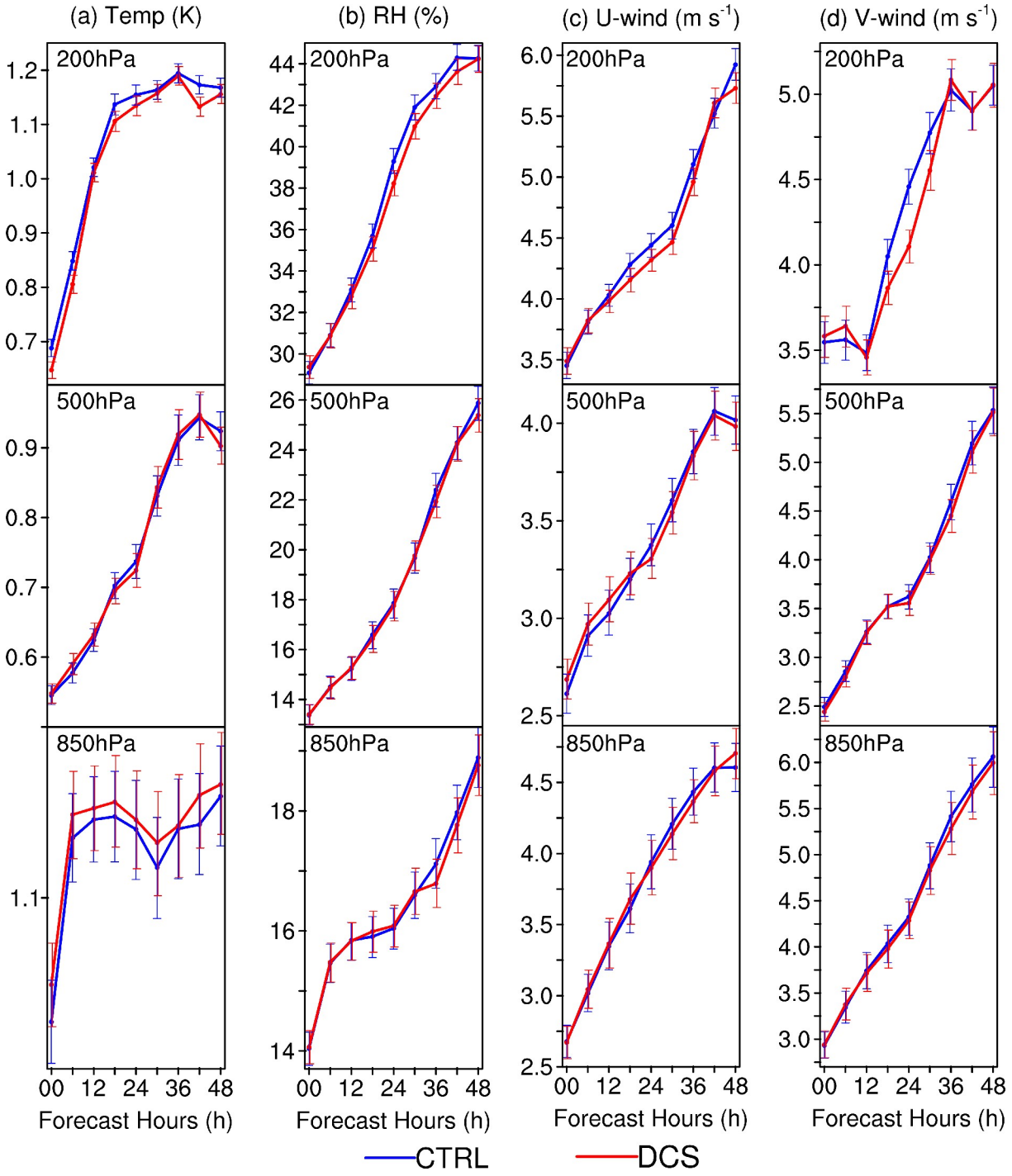

Fig. 7. Same as Fig. 6, but for Typhoon Lekima (2019).

Table 2. The averaged improve ratio at the upper (200 hPa), middle (500 hPa), and lower (850 hPa) troposphere in the two typhoon cases.

Case	Altitude	*T* (%)	RH (%)	*U* (%)	*V* (%)
Lekima (2019)	200 hPa	1.15	–0.41	0.99	1.20
	500 hPa	1.23	0.44	0.40	0.29
	850 hPa	–0.20	–0.23	0.20	0.33
Mitag (2019)	200 hPa	2.42	1.05	1.45	1.49
	500 hPa	–0.20	0.56	–0.27	1.34
	850 hPa	–0.78	0.27	–0.05	0.85

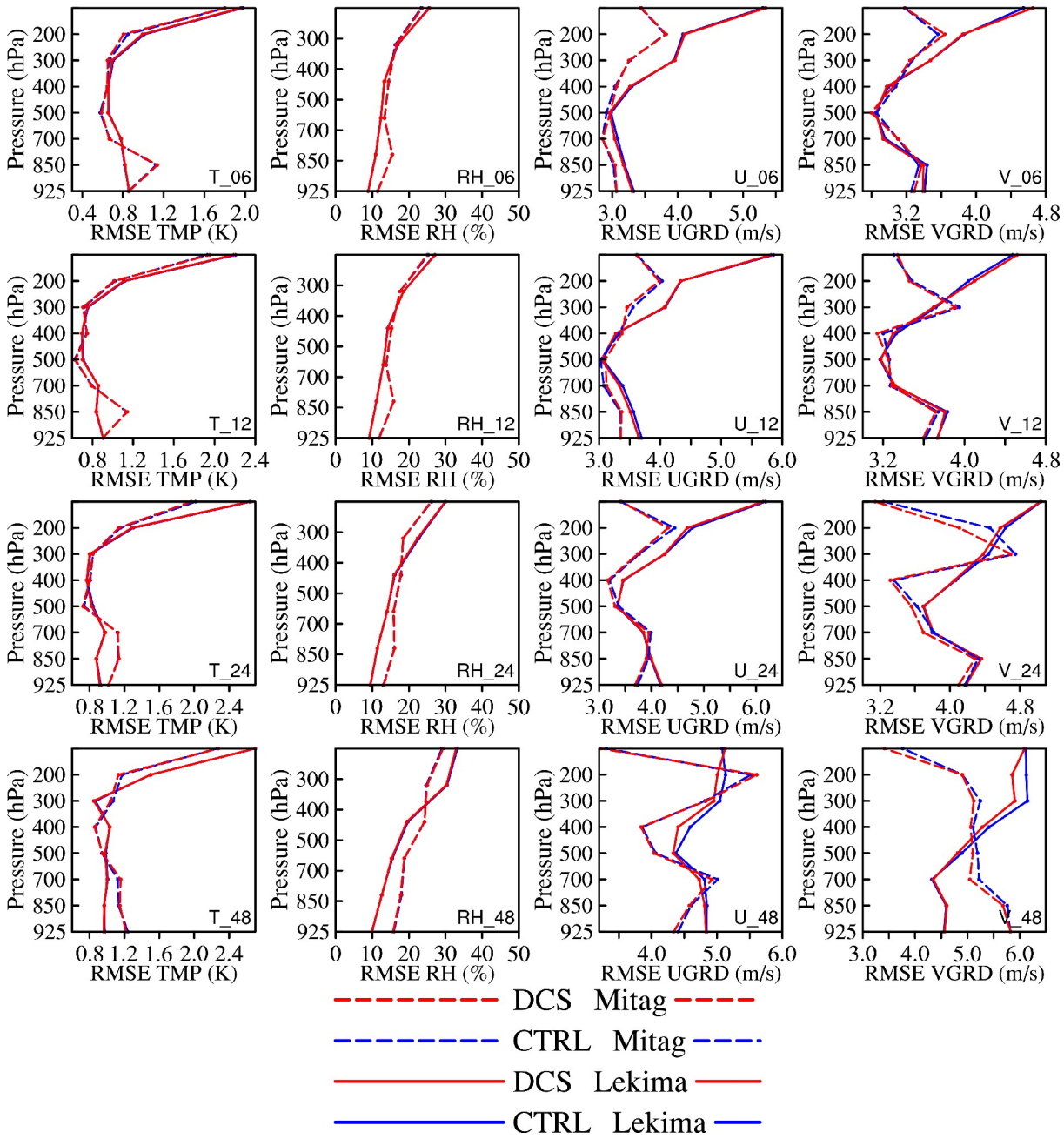

Fig. 8. The vertical profiles of the 6-h (first line), 12-h (second line), 24-h (third line), and 48-h (fourth line) forecasts of T (K, first column), RH (%, second column), U (m s^{-1}, third column), and V (m s^{-1}, fourth column) for Typhoons Lekima (2019, solid lines) and Mitag (2019, dashed lines) for the CTRL (blue) and DCS (red) experiments compared with ERA5.

low temporal resolution. Although it provides a lot of observations from MWTS-II, the increased number of observations in the DCS experiments cover only a part of the model domain, and the impacts are subtle after averaging over multiple forecasts and more than 10 000 grid points. Applying the DCS method to more MW sounders is likely to cause more significant differences.

5.2. *Averaged typhoon track and intensity forecast errors*

The impact of assimilating MWTS-II radiance data is evaluated by examining the 72-h forecasts from each analysis. The average absolute errors for track, CSLP, and MWS in the 72-h forecasts from the Lekima (2019) and Mitag (2019) cases are shown in Fig. 9, as verified against the best track from JTWC. The track and intensity results come from the output of the moving-nest domain.

On average, neither experiment produces superior forecasts. For the stronger typhoon, Lekima (2019), there are slight improvements in track forecasts as forecast time increases. The averaged reduction of track error for the DCS experiment is approximately 4.53% compared to the CTRL experiment. The improvements in track forecasts may be a result of assimilating more observations in the

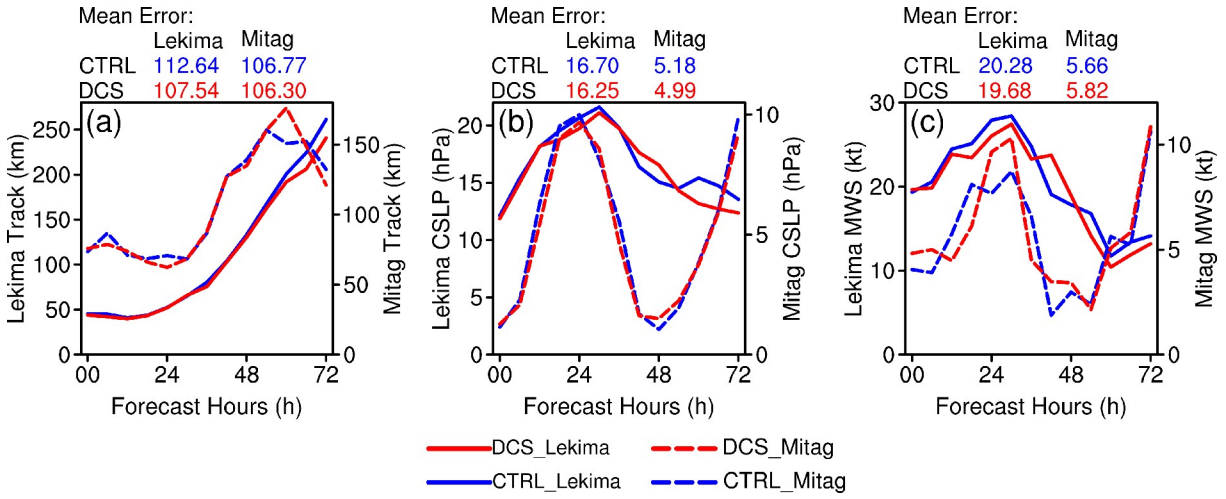

Fig. 9. The average absolute forecast errors of (a) track, (b) central sea level pressure, and (c) maximum wind speed as functions of forecast range from the two experiments, as verified against the best track from the JTWC. The error statistics are obtained from all 72-h forecasts for Typhoon Lekima (2019) and four 72-h forecasts for Typhoon Mitag (2019). The blue lines indicate CTRL experiments, and the red lines indicate DCS experiments. The solid lines indicate the results of Typhoon Lekima (2019) and correspond to the left *y*-axis, and the dashed lines indicate the results of Typhoon Mitag (2019) and correspond to the right *y*-axis. The averages of forecast time are the text on the top of the figures.

DCS experiment, which improves the environmental field and further increases the accuracy of the steering flow. CSLP and MWS are used to reflect the typhoon intensity forecast. For both typhoons, the intensity forecast errors continue to increase during the first 30 h of the forecast due to the typhoon intensification. However, in the 30-h to 48-h forecasts, the forecast errors decrease as the typhoon matures. After the 48-h forecast, the errors gradually increase again as the typhoon weakens. Both the CTRL and DCS experiments show this "increase–decrease–increase" trend of intensity forecast errors. The intensity forecasts are mixed. For Lekima (2019), except for the 42-h and 48-h forecasts, the DCS experiment has a smaller CSLP forecast error than the CTRL experiment. The maximum improvement of the DCS experiment CSLP forecast error is about 16.97%. Similar conclusions can be drawn for the MWS of Lekima (2019). For the weaker typhoon, Mitag (2019), the results are not as positive as for Lekima (2019). The CSLP forecast results is neutral, and the MWS forecast results is even negative. This may be attributed to the complexity of typhoon intensity forecasting (Wang and Wu, 2004; Yu et al., 2013; Ito, 2016).

The assimilation of FY-3D MWTS-II data using the DCS method slightly improves typhoons track forecasts on average and neutrally impacts intensity forecasts. These results may also be related to the slight increase of STDV in channel 5. As discussed in section 4.1, a small percentage of bad data may compromise the data impact or even cause a negative impact. It is essential to implement more stringent quality control steps when adding a large number of observations in order to minimize the impact of bad observations.

6. Impact analysis of Typhoon Lekima (2019)

To further explore the impact on typhoons of assimilating FY-3D MWTS-II data, the analysis and forecast results of two experiments are diagnosed, using the Lekima (2019) case as an example. Figure 10a shows the best track from JTWC with the 72-h track forecasts starting at 1800 UTC 7 August 2019 from the two experiments. According to the best track, Typhoon Lekima (2019) consistently moves northwesterly. Compared with the best track, the typhoon speeds of both experiments are slower, about 6 h behind after the 42-h forecast. However, the tracks of the DCS experiment are closer to the best track at most time steps. The landfall time is about 1 h earlier than the CTRL experiment, and the landfall location is also closer to the best track. Due to the tracks in both experiments generally lagging behind the best track, the forecast intensities are too weak before landfall (1745 UTC 9 August) and too strong after landfall. On average, CSLP and MWS in the DCS experiments are closer to the best track.

6.1. *Large-scale circulation analysis*

The quantity and quality of observations directly affect the analysis field. For MWTS-II data, the most influential analysis variable is temperature. Figure 11 shows the temperature analysis increments with the distribution of assimilated observations at 0600 UTC and 1800 UTC on 7 August 2019, which are the two time steps with the largest number of FY-3D observations in a day. In general, the locations of MWTS-II observations are always associated with temperature analysis increments. The temperature analysis increments of the CTRL and DCS experiments are consistently distributed in regions without satellite observations, such as 123°–130°E and 10°–15°N at 0600 UTC (Figs. 11a and c) and the Korean Peninsula at 1800 UTC (Figs. 11b and d), and are brought by conventional observations. Compared to the CTRL experiment, by using the DCS method, more obser-

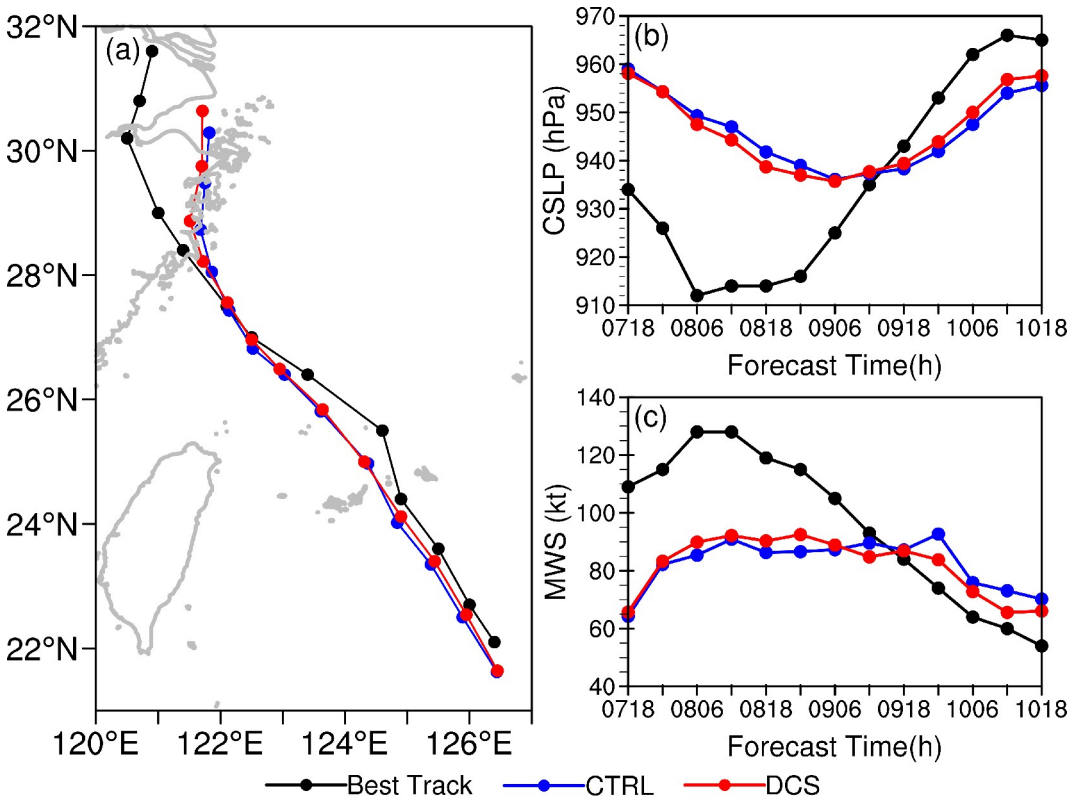

Fig. 10. The Typhoon Lekima (2019) forecast (a) tracks, (b) CSLP (hPa), and (c) MWS (kt) of the CTRL experiment (blue) and the DCS experiment (red) started at 1800 UTC 7 August 2019. The best track (black) is from the JTWC.

vations are assimilated and more temperature information is included. The differences in temperature analysis between the CTRL and DCS experiments are shown in Figs. 11e and f. In the first analysis cycle (Fig. 11e), the temperature differences correspond to additional observation distributions and are only influenced by the different observations brought by the DCS method. After several analysis cycles, the temperature differences do not exactly correspond to the observed distributions (Fig. 11f), and differences also appear in the center of the typhoon. This is because the model adjustment during assimilation cycles transfers the previous temperature information to the center of the typhoon, which will further affect the intensity and location of the typhoon.

The analysis increments of geopotential height and the difference in geopotential height analysis fields are shown in Fig. 12. Similar to temperature, the analysis increments of geopotential height are distributed consistently with the analysis increments of temperature. In the first analysis cycle, both experiments have large positive geopotential height increments in eastern China and the Korean peninsula and have large negative increments in the northeast of the typhoon, which would have shifted the depression of typhoon Lekima (2019) to the northeast. The DCS experiment has larger increments, and this influence is stronger because there are more MWTS-II observations, so the typhoon position in the DCS experiment at this time step is more northeastward than in the CTRL experiment, which is consistent with the results shown in Fig. 10. In the third analysis cycle, the difference in the analysis increment is not very obvious due to the decrease in the number of assimilated observations compared to the first analysis cycle. The differences in geopotential height analysis fields show that the negative increment left by the first analysis in the northeast of the typhoon is still passed to the third analysis after several cycles, which places the typhoon position more to the northeast at this analysis time step. This influence is gradually spread to the inner core of the typhoon, which will be discussed in section 6.2.

A similar pattern is found for sea level pressure (Fig. 13). Since the main impact heights of the assimilated MWTS-II channels are in the upper atmosphere, the radiance observations have a relatively limited impact on sea level pressure. However, after the first analysis cycle, there is still a decrease of sea level pressure on the northeast side of the typhoon. And after several analysis cycles, the positive sea level pressure increments in the northwest of the typhoon and the negative pressure increments in the northeast will also shift the typhoon to the northeast. The changes in both geopotential height and sea level pressure increments are consistent with the northeast-oriented track forecast results.

6.2. *Typhoon structure analysis*

To further analyze the improvement of forecasting

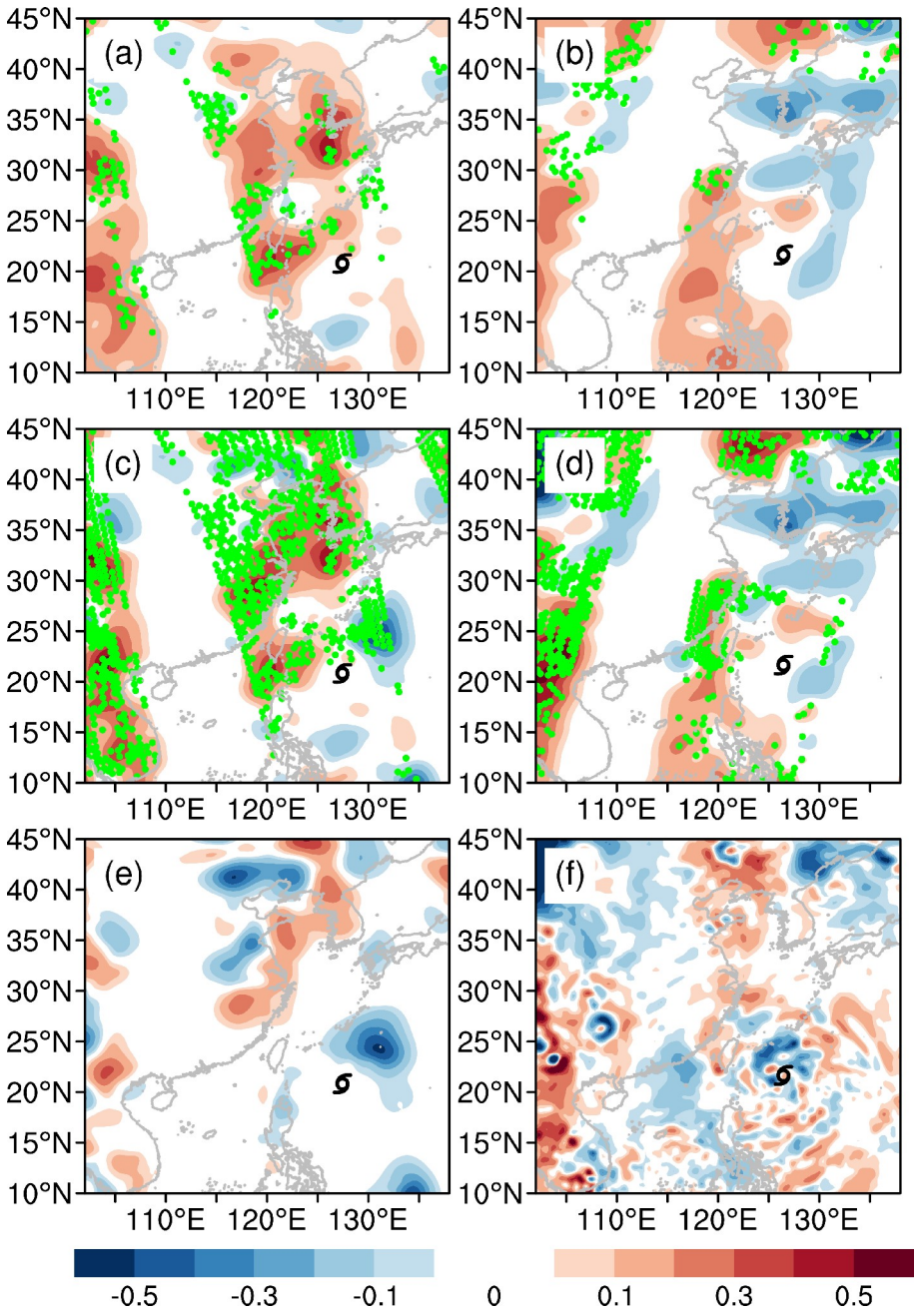

Fig. 11. The analysis increments of temperature (units: K) for the (a), (b) CTRL and (c), (d) DCS experiments, and (e), (f) the temperature difference between the CTRL and DCS experiment analysis fields (DCS minus CTRL, units: K) at (a–c) 0600 UTC and (d–f) 1800 UTC 7 August 2019. The green dots indicate the of channel-7 data assimilated in each experiment. The Typhoon Lekima (2019) center from the best track is marked as black at each time.

typhoon intensity using the DCS method, analysis fields of the zonal vertical sections, including horizontal wind and temperature anomalies, across the center of Lekima (2019) at different analysis time steps are shown in Fig. 14. In the first analysis, the observations are outside the typhoon and could not directly impact the typhoon structure. So, the temperature anomalies are the same for both experiments, and the typhoon intensities are slightly weaker than the NCEP FNL (Final) Operational Global Analysis. The slight difference between the CTRL and DCS experiments starts to show up in the second analysis cycle, and the typhoon intensities start to be stronger than the FNL. After the third analysis, the typhoon intensity of the DCS experiment is gradually strengthened by continuous adjustments of the additional observations. The warm core is enhanced and deeper, and the wind field is more symmetrical. It is the rapid strengthening phase of the typhoon, and there are still some limitations to enhancing typhoon intensity after assimilating MWTS-II

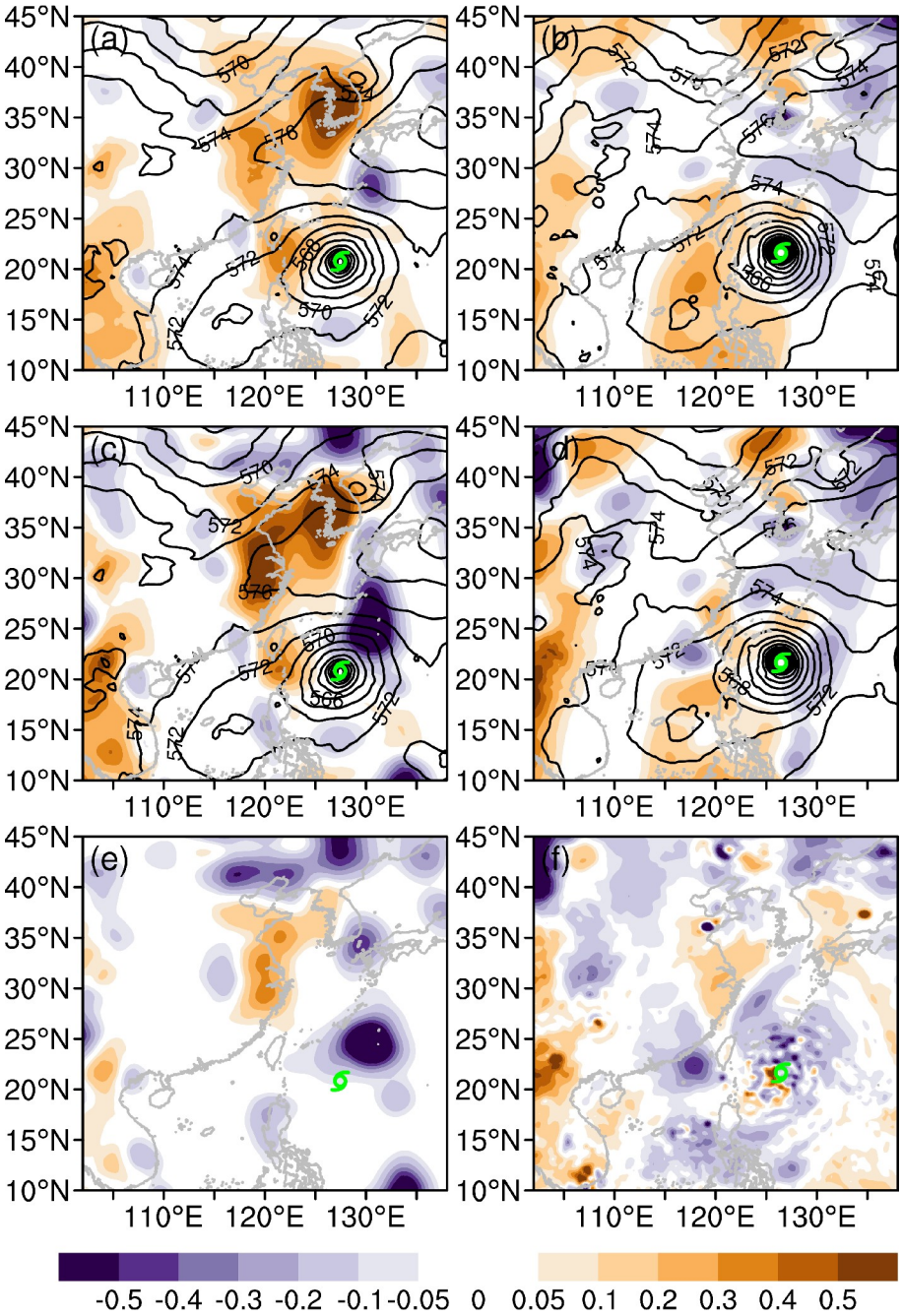

Fig. 12. The analysis increments of geopotential height (shading, units: $m^2\ s^{-2}$) and the analysis fields of geopotential height (contours, units: $m^2\ s^{-2}$; contours every 2 $m^2\ s^{-2}$) for the (a), (b) CTRL and (c), (d) DCS experiments, and (e), (f) the geopotential height difference between the CTRL and DCS experiment analysis fields (DCS minus CTRL, units: $m^2\ s^{-2}$) at (a–c) 0600 UTC 7 August 2019 and (d–f) 1800 UTC 7 August 2019. The Typhoon Lekima (2019) center from the best track is marked as green at each time.

only. But the CSLP of the DCS experiment is closer to the best track compared to the CTRL experiment. After the fourth analysis, the stronger intensity of the typhoon in the DCS experiment is apparent. Although MWTS-II observations are distributed at the outer part of the typhoon, the typhoon intensity of the analyzed field is improved, which may be due to the continuous adjustment of the model and the accumulation of observation information by several cycles of assimilating additional observations brought by the DCS method. More temperature information is passed to the typhoon center, improving the typhoon intensity analysis.

7. Conclusions and discussion

Precipitation detection is necessary for the radiance

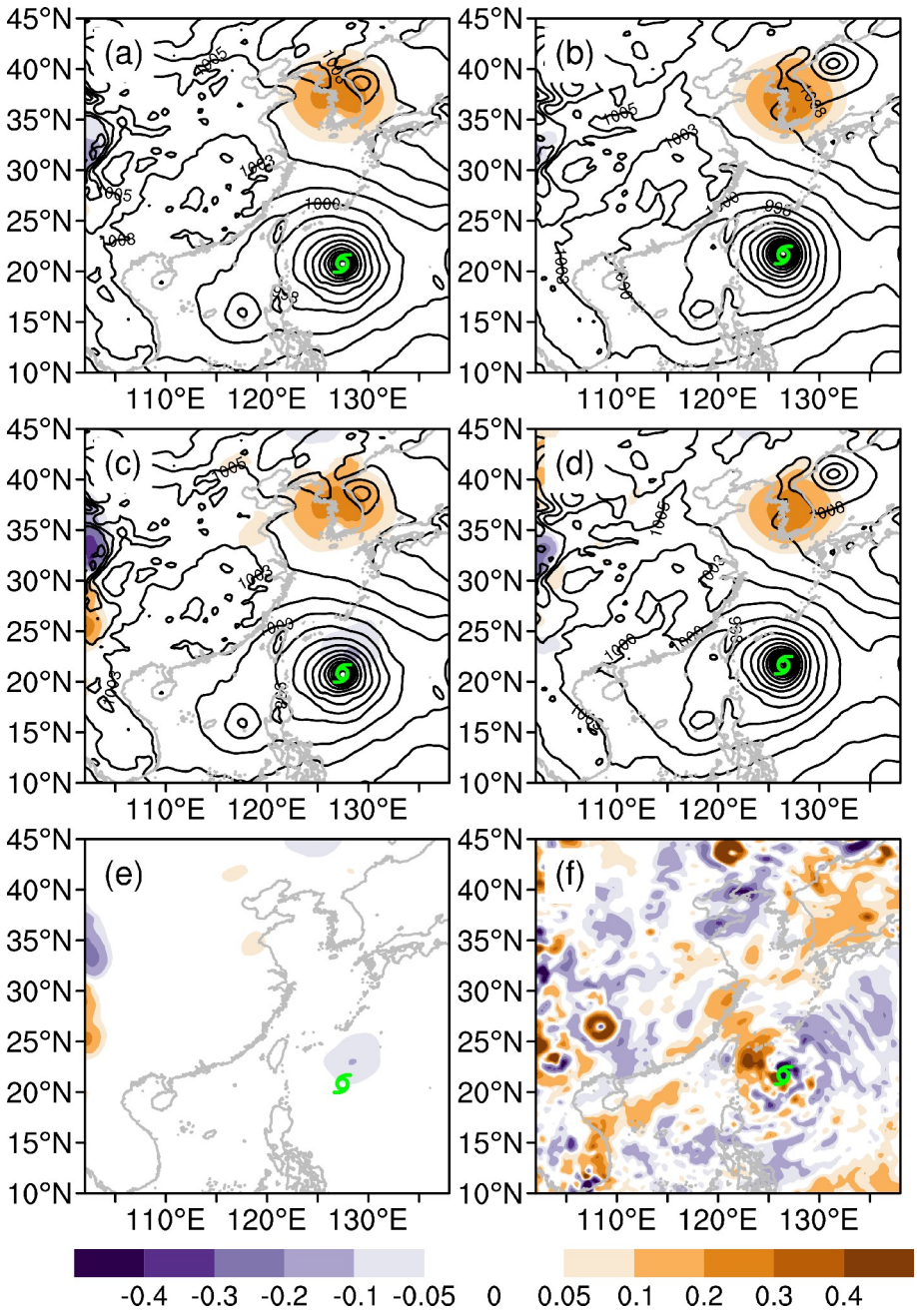

Fig. 13. Same as Fig. 10, but for sea level pressure (units: hPa, contours every 2 hPa).

assimilation because the uncertainties in clouds and precipitation would affect the radiative transfer and observation errors. The traditional precipitation detection method for microwave only detects clouds and precipitation horizontally without considering the three-dimensional distribution of clouds. To more accurately detect the vertical distribution of precipitation, a 3D precipitation detection method called DCS, which considers near-real-time 3D cloud distribution to dynamically select channels above precipitation clouds, was employed. To evaluate the influence of the DCS method when FY-3D MWTS-II data are assimilated, cycled assimilation experiments with a simplified observing system and a regional configuration were carried out on two typhoon cases.

By supplementing the channel information above the precipitation cloud, the DCS method increases the amount of FY-3D MWTS-II data available for assimilation without affecting the observation quality, as proven by the OMB statistic and Gaussian PDF of the DCS experiments. The additional radiance data made usable by the DCS method provides additional benefits for typhoon analysis and forecasting. The temperature analysis first responds around the additional radiance information and then is transferred to the typhoon core area after several assimilation cycles. Therefore, a tighter eye, a stronger warm core, and a more symmetrical wind field with deeper convection are captured. The improve-

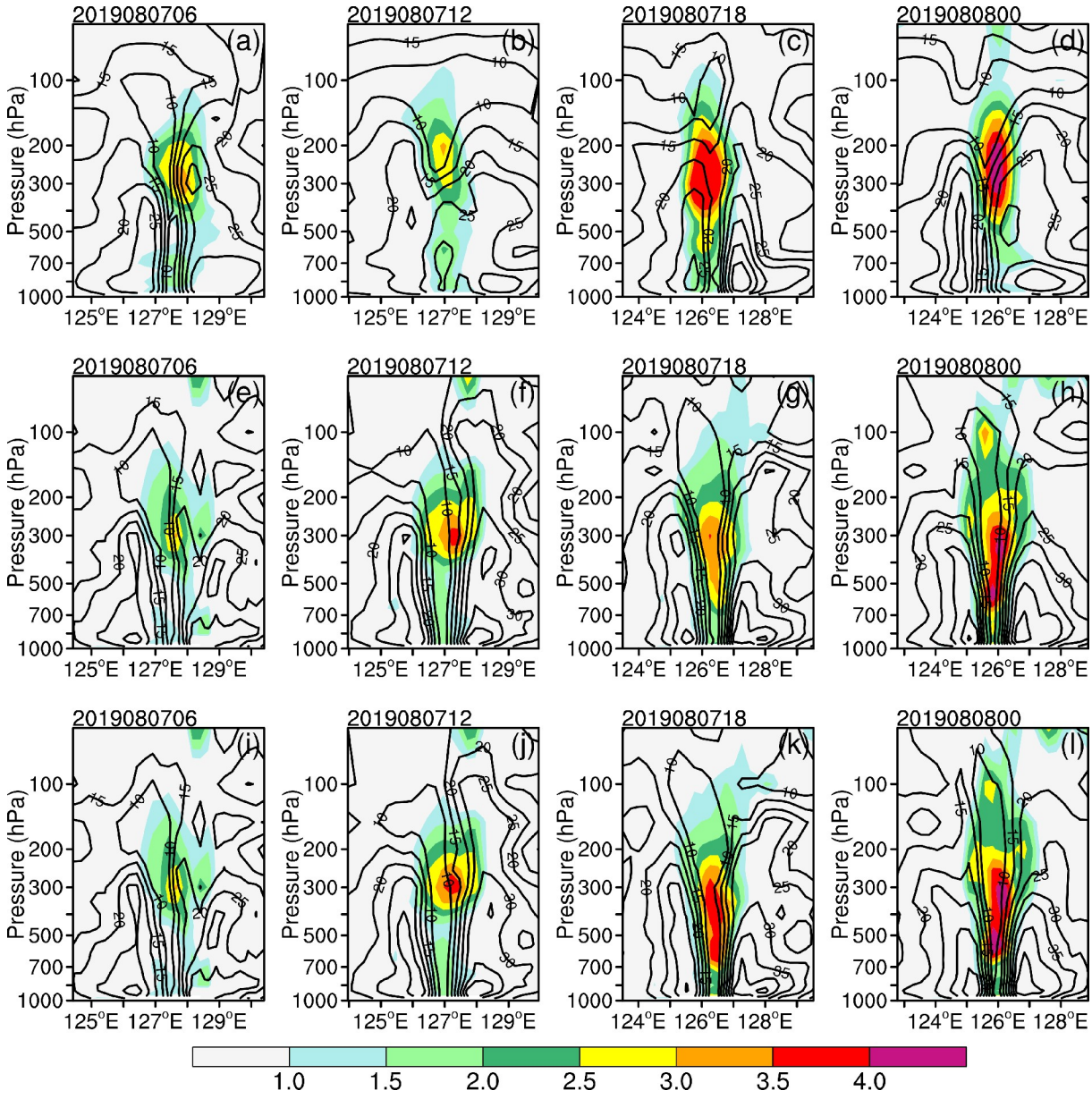

Fig. 14. Zonal vertical section of wind (m s^{-1}, the black contours; contours every 5 m s^{-1}) and the temperature anomaly (K, the color shaded contours) of (a–d) FNL, (e–f) CTRL, and (i–l) DCS analysis at (a), (e), (i) 0600 UTC, (b), (f), (j) 1200 UTC, (c), (g), (k) 1800 UTC 7 August 2019 and (d), (h), (l) 0000 UTC 8 August 2019.

ments in the analysis impact the subsequent forecasts. With more upper channels assimilated, the forecast improvements are concentrated in the upper troposphere. The cycle-average root-mean-square errors (RMSE) of prognostic variables are reduced by 1.7%, leading to an average reduction of 4.53% in typhoon track forecast errors. The improvement in the typhoon intensity forecast was neutral.

This study preliminarily shows the application potential of increasing FY-3 satellite data utilization. Based on these results, it is essential to further evaluate the impacts of the DCS method in a full system with numerous IR and MW satellite observations already assimilated. The evaluation of the DCS method in the global operational GRAPES system with four-dimensional variational data assimilation is underway. This system has reasonable and mature assimilation parameters for all satellites, and the results could be more convincing.

The DCS method was first applied to MWTS-II because it has a more urgent need for reasonable and accurate precipitation detection in the absence of window channels. Since only one MW sounder is assimilated for now, the impacts on forecasts are subtle. Future research could concentrate on combining multiple MWTS-II when other FY-3 series polar-orbiting satellites are launched. The DCS method is likely to apply to AMSU-A and ATMS data as well, which will bring more useful information. Key issues of extending the DCS method to other instruments include testing the generalizability of lookup tables, etc., which

need further research. The DCS method shows the potential for better use of radiance information around precipitation without the all-sky method. It makes sense to use as many observations as possible that are not affected by precipitation before the all-sky assimilation of MW temperature channels can be fully operationally applied.

When building the DCS lookup tables, only the absorption of cloud liquid water was considered. If the scattering of precipitation particles could be considered, the lower channels containing richer cloud information can be better assimilated and may bring more improvements. Furthermore, a slight increase in the STDV of channel 5 was found, which may indicate the DCS method introduces too many observations for channel 5. More observations are more likely to be influenced by the surface or clouds. Therefore, relevant actions, such as adding additional surface quality control or tightening the diff thresholds for channel 5, are worth exploring.

Acknowledgements. This work is jointly sponsored by the National Key Research and Development Program of China (Grant Nos. 2018YFC1506701 and 2017YFC1502102) and the National Natural Science Foundation of China (Grant No. 41675102). The authors would also like to thank three reviewers for their many valuable comments to help us improve the quality of this paper.

Data statement. The Level-1c (L1c) datasets of the FY-3D MWTS-II and the BT of MERSI-2 were provided by the NSMC (http://data.nsmc.org.cn). The best tracks of JTWC were from International Best Track Archive for Climate Stewardship (https://www.ncei.noaa.gov). The NCEP/GFS analysis was obtained from NOAA (https://www.ncdc.noaa.gov). The NCEP FNL was obtained from NCAR (https://rda.ucar.edu/datasets/ds083.2). The ERA5 was obtained from ECMWF (https://cds.climate.copernicus.eu/#!/home).

REFERENCES

Auligné, T., and A. P. McNally, 2007: Interaction between bias correction and quality control. *Quart. J. Roy. Meteor. Soc.*, **133**, 643–653, https://doi.org/10.1002/qj.57.

Bauer, P., A. J. Geer, P. Lopez, and D. Salmond, 2010: Direct 4D-Var assimilation of all-sky radiances. *Part I: Implementation. Quart. J. Roy. Meteor. Soc.*, **136**, 1868–1885, https://doi.org/10.1002/qj.659.

Bauer, P., A. Thorpe, and G. Brunet, 2015: The quiet revolution of numerical weather prediction. *Nature*, **525**, 47–55, https://doi.org/10.1038/nature14956.

Buehner, M., P. L. Houtekamer, C. Charette, H. L. Mitchell, and B. He, 2010: Intercomparison of variational data assimilation and the ensemble kalman filter for global deterministic NWP. Part I: Description and single-observation experiments. *Mon. Wea. Rev.*, **138**, 1550–1566, https://doi.org/10.1175/2009MWR3157.1.

Carminati, F., N. Atkinson, B. Candy, and Q. F. Lu, 2021: Insights into the microwave instruments onboard the Fengyun 3D satellite: Data quality and assimilation in the met office NWP system. *Adv. Atmos. Sci.*, **38**, 1379–1396, https://doi.org/10.1007/s00376-020-0010-1.

Eyre, J. R., S. J. English, and M. Forsythe, 2020: Assimilation of satellite data in numerical weather prediction. Part I: The early years. Quart. *J. Roy. Meteor. Soc.*, **146**, 49–68, https://doi.org/10.1002/qj.3654.

Geer, A. J., and P. Bauer, 2011: Observation errors in all-sky data assimilation. *Quart. J. Roy. Meteor. Soc.*, **137**, 2024–2037, https://doi.org/10.1002/qj.830.

Geer, A. J., and Coauthors, 2017: Assimilating observations sensitive to cloud and precipitation. Technical memorandum, *Proc. 46th Science Advisory Committee*, Shinfield Park, Reading, UK, ECMWF, https://doi.org/10.21957/sz7cr1dym.

Geer, A. J., and Coauthors, 2018: All-sky satellite data assimilation at operational weather forecasting centres. *Quart. J. Roy. Meteor. Soc.*, **144**, 1191–1217, https://doi.org/10.1002/qj.3202.

Geer, A., N. Bormann, K. Lonitz, P. Weston, R. Forbes, and S. English, 2019: Recent progress in all-sky radiance assimilation. ECMWF Newslette No. 161, 8 pp.

Grody, N., J. Zhao, R. Ferraro, F. Z. Weng, and R. Boers, 2001: Determination of precipitable water and cloud liquid water over oceans from the NOAA 15 advanced microwave sounding unit. *J. Geophys. Res.*, **106**, 2943–2953, https://doi.org/10.1029/2000JD900616.

Guidard, V., N. Fourrié, P. Brousseau, and F. Rabier, 2011: Impact of IASI assimilation at global and convective scales and challenges for the assimilation of cloudy scenes. *Quart. J. Roy. Meteor. Soc.*, **137**, 1975–1987, https://doi.org/10.1002/qj.928.

Hersbach, H., and Coauthors, 2020: The ERA5 global reanalysis. *Quart. J. Roy. Meteor. Soc.*, **146**, 1999–2049, https://doi.org/10.1002/qj.3803.

Hong, S.-Y., and J.-O. J. Lim, 2006: The WRF single-moment 6-class microphysics scheme (WSM6). *Journal of the Korean Meteorological Society*, **42**, 129–151.

Hong, S.-Y., Y. Noh, and J. Dudhia, 2006: A new vertical diffusion package with an explicit treatment of entrainment processes. *Mon. Wea. Rev.*, **134**, 2318–2341, https://doi.org/10.1175/MWR3199.1.

Hsiao, L.-F., D.-S. Chen, Y.-H. Kuo, Y.-R. Guo, T.-C. Yeh, J.-S. Hong, C.-T. Fong, and C.-S. Lee, 2012: Application of WRF 3DVAR to operational typhoon prediction in Taiwan: Impact of outer loop and partial cycling approaches. *Wea. Forecasting*, **27**, 1249–1263, https://doi.org/10.1175/WAF-D-11-00131.1.

Iacono, M. J., J. S. Delamere, E. J. Mlawer, M. W. Shephard, S. A. Clough, and W. D. Collins, 2008: Radiative forcing by long-lived greenhouse gases: Calculations with the AER radiative transfer models. *J. Geophys. Res.*, **113**, D13103, https://doi.org/10.1029/2008JD009944.

Ito, K., 2016: Errors in tropical cyclone intensity forecast by RSMC tokyo and statistical correction using environmental parameters. *SOLA*, **12**, 247–252, https://doi.org/10.2151/sola.2016-049.

Lee, J.-R., J. Li, Z. L. Li, P. Wang, and J. L. Li, 2019: ABI water vapor radiance assimilation in a regional NWP model by accounting for the surface impact. *Earth and Space Science*, **6**, 1652–1666, https://doi.org/10.1029/2019EA000711.

Li, J., and X. L. Zou, 2013: A quality control procedure for FY-3A MWTS measurements with emphasis on cloud detection using VIRR cloud fraction. *J. Atmos. Oceanic Technol.*, **30**, 1704–1715, https://doi.org/10.1175/jtech-d-12-00164.1.

Li, J., and X. L. Zou, 2014: Impact of FY-3A MWTS radiances

on prediction in GRAPES with comparison of two quality control schemes. *Frontiers of Earth Science*, **8**, 251–263, https://doi.org/10.1007/s11707-014-0405-3.

Li, J., and G. Q. Liu, 2016a: Assimilation of Chinese Fengyun-3B Microwave Temperature Sounder radiances into the Global GRAPES system with an improved cloud detection threshold. *Frontiers of Earth Science*, **10**, 145–158, https://doi.org/10.1007/s11707-015-0499-2.

Li, J., and G. Q. Liu, 2016b: Direct assimilation of Chinese FY-3C Microwave Temperature Sounder-2 radiances in the global GRAPES system. *Atmospheric Measurement Techniques*, **9**, 3095–3113, https://doi.org/10.5194/amt-9-3095-2016.

Liu, Z.-Q., and F. Rabier, 2002: The interaction between model resolution, observation resolution and observation density in data assimilation: A one-dimensional study. *Quart. J. Roy. Meteor. Soc.*, **128**, 1367–1386, https://doi.org/10.1256/003590002320373337.

Lu, Q. F., W. Bell, P. Bauer, N. Bormann, and C. Peubey, 2011: Characterizing the *FY-3A* microwave temperature sounder using the ECMWF model. *J. Atmos. Oceanic Technol.*, **28**, 1373–1389, https://doi.org/10.1175/jtech-d-10-05008.1.

Migliorini, S., and B. Candy, 2019: All-sky satellite data assimilation of microwave temperature sounding channels at the Met Office. *Quart. J. Roy. Meteor. Soc.*, **145**, 867–883, https://doi.org/10.1002/qj.3470.

Parrish, D. F., and J. C. Derber, 1992: The national meteorological center's spectral statistical-interpolation analysis system. *Mon. Wea. Rev.*, **120**, 1747–1763, https://doi.org/10.1175/1520-0493(1992)120<1747:TNMCSS>2.0.CO;2.

Qin, L. Y., Y. D. Chen, T. L. Yu, G. Ma, Y. Guo, and P. Zhang, 2020: Dynamic channel selection of microwave temperature sounding channels under cloudy conditions. *Remote Sensing*, **12**, 403, https://doi.org/10.3390/rs12030403.

Saunders, R., M. Matricardi, and P. Brunel, 1999: An improved fast radiative transfer model for assimilation of satellite radiance observations. *Quart. J. Roy. Meteor. Soc.*, **125**, 1407–1425, https://doi.org/10.1002/qj.1999.49712555615.

Sun, J. Z., H. L. Wang, W. X. Tong, Y. Zhang, C.-Y. Lin, and D. M. Xu, 2016: Comparison of the impacts of momentum control variables on high-resolution variational data assimilation and precipitation forecasting. *Mon. Wea. Rev.*, **144**, 149–169, https://doi.org/10.1175/MWR-D-14-00205.1.

Tiedtke, M., 1989: A comprehensive mass flux scheme for cumulus parameterization in large-scale models. *Mon. Wea. Rev.*, **117**, 1779–1800, https://doi.org/10.1175/1520-0493(1989)117<1779:ACMFSF>2.0.CO;2.

Tong, M. J., Y. Q. Zhu, L. J. Zhou, E. Liu, M. Chen, Q. H. Liu, and S.-J. Lin, 2020: Multiple hydrometeors all-sky microwave radiance assimilation in FV3GFS. *Mon. Wea. Rev.*, **148**, 2971–2995, https://doi.org/10.1175/MWR-D-19-0231.1.

Wang, P., and Coauthors, 2015: Assimilation of thermodynamic information from advanced infrared sounders under partially cloudy skies for regional NWP. *J. Geophys. Res.*, **120**, 5469–5484, https://doi.org/10.1002/2014JD022976.

Wang, P., J. Li, Z. L. Li, A. H. N. Lim, J. L. Li, T. J. Schmit, and M. D. Goldberg, 2017: The impact of cross-track infrared sounder (CrIS) cloud-cleared radiances on hurricane joaquin (2015) and matthew (2016) forecasts. *J. Geophys. Res.*, **122**, 13 201–13 218, https://doi.org/10.1002/2017JD027515.

Wang, Y., and C.-C. Wu, 2004: Current understanding of tropical cyclone structure and intensity changes – a review. *Meteorol. Atmos. Phys.*, **87**, 257–278, https://doi.org/10.1007/s00703-003-0055-6.

Weng, F. Z., L. M. Zhao, R. R. Ferraro, G. Poe, X. F. Li, and N. C. Grody, 2003: Advanced microwave sounding unit cloud and precipitation algorithms. *Radio Sci.*, **38**, 8068, https://doi.org/10.1029/2002RS002679.

Weng, F. Z., T. Zhu, and B. H. Yan, 2007: Satellite data assimilation in numerical weather prediction models. Part II: Uses of rain-affected radiances from microwave observations for hurricane vortex analysis. *J. Atmos. Sci.*, **64**, 3910–3925, https://doi.org/10.1175/2006jas2051.1.

Weston, P., A. J. Geer, and N. Bormann, 2019: Investigations into the assimilation of AMSU-A in the presence of cloud and precipitation. EUMETSAT/ECMWF Fellowship Programme Research Rep. 50, 42 pp, https://doi.org/10.21957/ewahn9ce.

Xie, Y. H., S. Y. Fan, M. Chen, J. C. Shi, J. Q. Zhong, and X. Y. Zhang, 2019: An assessment of satellite radiance data assimilation in RMAPS. *Remote Sensing*, **11**, 54, https://doi.org/10.3390/rs11010054.

Yu, H., P. Y. Chen, Q. Q. Li, and B. Tang, 2013: Current capability of operational numerical models in predicting tropical cyclone intensity in the Western North Pacific. *Wea. Forecasting*, **28**, 353–367, https://doi.org/10.1175/WAF-D-11-00100.1.

Zhang, M. Y., L. F. Zhang, B. Zhang, J. P. Guan, and W. You, 2019a: Assimilation of MWHS and MWTS radiance data from the FY-3A satellite with the POD-3DEnVar method for forecasting heavy rainfall. *Atmospheric Research*, **219**, 95–105, https://doi.org/10.1016/j.atmosres.2018.12.023.

Zhang, P., and Coauthors, 2019b: Latest progress of the Chinese meteorological satellite program and core data processing technologies. *Adv. Atmos. Sci.*, **36**, 1027–1045, https://doi.org/10.1007/s00376-019-8215-x.

Zhou, Y. P., K.-M. Lau, O. Reale, and R. Rosenberg, 2010: AIRS impact on precipitation analysis and forecast of tropical cyclones in a global data assimilation and forecast system. *Geophys. Res. Lett.*, **37**, L02806, https://doi.org/10.1029/2009gl041494.

Zhu, Y. Q., and Coauthors, 2016: All-sky microwave radiance assimilation in NCEP's GSI analysis system. *Mon. Wea. Rev.*, **144**, 4709–4735, https://doi.org/10.1175/MWR-D-15-0445.1.

Zou, X., F. Weng, B. Zhang, L. Lin, Z. Qin, and V. Tallapragada, 2013: Impacts of assimilation of ATMS data in HWRF on track and intensity forecasts of 2012 four landfall hurricanes. *J. Geophys. Res.*, **118**, 11 558–11 576, https://doi.org/10.1002/2013JD020405.